ISSN 0021-3640, JETP Letters, 2023, Vol. 117, No. 2, pp. 104–110. © Pleiades Publishing, Inc., 2023.
Russian Text © The Author(s), 2023, published in Pis'ma v Zhurnal Eksperimental'noi i Teoreticheskoi Fiziki, 2023, Vol. 117, No. 2, pp. 107–114.

OPTICS
AND LASER PHYSICS

Determination of the Most Important Parameters of a Metal Irradiated by an Ultrashort Laser Pulse

N. A. Inogamov[a, b, c, *] (ORCID: 0000-0002-7703-4415), V. A. Khokhlov[a, c] (ORCID: 0000-0001-9126-0243), S. A. Pomashevskii[c] (ORCID: 0000-0001-6061-6702), Yu. V. Petrov[a], V. V. Zhakhovsky[b, c] (ORCID: 0000-0001-6620-6616), and S. I. Ashitkov[c] (ORCID: 0000-0003-3655-4585)

[a] *Landau Institute for Theoretical Physics, Russian Academy of Sciences, Chernogolovka, Moscow region, 142432 Russia*
[b] *Dukhov All-Russia Research Institute of Automatics, Moscow, 127055 Russia*
[c] *Joint Institute for High Temperatures, Russian Academy of Sciences, Moscow, 125412 Russia*
**e-mail: nailinogamov@gmail.com*

Received November 16, 2022; revised November 26, 2022; accepted December 1, 2022

Ultrashort laser pulses with a duration from several to about a thousand cycles have significant importance in modern science and engineering. Such a pulse transfers a metal to an excited two-temperature state with hot electrons where the temperature of the electron subsystem T_e is much higher than the temperature of the ion subsystem T_i. The thermal conductivity in such systems differs from well-known reference values. The thermal conductivity κ and the energy exchange rate between the electron and ion subsystems α are the key parameters of the two-temperature model, which are still poorly studied, although studies of these parameters, particularly α, are numerous. New theoretical and experimental results that make it possible to determine the parameters κ and α for gold have been reported in this work.

DOI: 10.1134/S0021364022603050

1. INTRODUCTION

Ultrashort laser pulses are widely used in plasmonics [1, 2], for micro- and nanoprocessing of the surface (structuring [2–5] and hardening [6]), and for the production of colloidal solutions of nanoparticles [7]. Consequently, the physics of action of ultrashort laser pulses on metals is of great interest. Isolated atoms can exist in the ground and excited states. The action of ultrashort laser pulses on condensed matter results in the appearance of an analog of an excited state. Photoprocesses are responsible for the relaxation of excitation, whereas relaxation in metals is due to the Cherenkov emission of phonons by supersonic electrons [8, 9]. The electron–ion relaxation coefficient α, which is often denoted as g [10], is related to this process.

The electromagnetic field of light lasers penetrates into metals only in a thin skin layer with a thickness of $d_{\text{skin}} = 10–20$ nm because the plasma frequency is higher than the laser frequency. Therefore, the cooling of the skin layer caused by the electron thermal conductivity plays a very important role in the kinetics of relaxation (from the nonequilibrium two-temperature to equilibrium one-temperature ($T_e = T_i$) state) in films thicker than the skin layer and in bulk samples. Thus, the exchange coefficient α and thermal conductivity κ determine the physics of action of ultrashort laser pulses. The aim of this work is to determine these parameters.

2. ELECTRON–PHONON COUPLING

The important role of the electron–phonon coupling in the relaxation of electron excitation was emphasized already in the first works [8, 9]. Information on the relaxation of electrons was obtained in the 1980s and 1990s in experiments on temperature-induced change in the reflectivity (below, transient thermoreflectance (TTR)) [11–14]. The electron subsystem was heated slightly in those experiments: the electron temperature T_e was higher than room temperature by no more than a few hundred kelvin. Values of $(2–4) \times 10^{16}$ W K^{-1} m^{-3} were obtained for the parameter α in gold.

In more recent works [15–17], first, an ultrashort electron or X-ray probe pulse was used for the diagnostic after the main femtosecond optical pump pulse, and the current ion temperature T_i was determined from the thermal broadening of lines of ions in the lattice; and, second, reflected radiation and radiation transmitted through the film was detected and the energy absorbed by the film was accurately determined. The optical characteristics of gold in the two-temperature state were determined from the reflection and transmission coefficients [18–22]. The onset time

of melting of an ultrathin (with a thickness of $d_f \sim d_{skin}$) film was determined [20]; see also the description of melting of gold in [23].

Laser energies and, correspondingly, maximum electron temperatures T_e in [11–14] were low, whereas the authors of [15–17, 24] introduced high energies in ultrathin films with a thickness of $d_f \sim d_{skin}$, so that the melting (see [25–27]) and ablation [27–29] of films occurred.

Calculations and measurements of the coefficient α seemed satisfactory before (a) works [30–32], (b) experiments [33, 34] with plotting of Laue diffraction patterns with a relativistic electron beam on an ultrathin (35 nm) gold single-crystal film irradiated by a femtosecond laser, and (c) molecular dynamics simulation [35, 36] to interpret experiments reported in [33]. A significant decrease in the coefficient α was recently (September 2022) mentioned in [37].

According to [30], the situation with the coefficient α is dramatic. Indeed, $\alpha(T_e = 15\ \text{kK})$ values calculated in different theoretical works cited in [30, Fig. 1b] differ by a factor of 7. Some of these calculations are based on a generalization [10, 38] proposed in [38]. This is a generalization to multiband metals of the single-band Allen approach [39]:

$$\alpha(T_e) = \frac{\pi\hbar k_B \lambda\langle\omega^2\rangle}{g_\Sigma(\varepsilon_F)} \int (g_\Sigma(\varepsilon))^2 (-\partial f_F/\partial\varepsilon) d\varepsilon, \qquad (1)$$

where $g_\Sigma(\varepsilon)$ is the total electron density of states; $f_F(\varepsilon;\mu(T_e),T_e)$ is the Fermi distribution of single-electron states in the energy ε; $\mu(T_e)$ is the chemical potential, which is determined from the condition of normalization to the number of electrons (the total number of s and d electrons in gold is 11; see, e.g., [26]); and ε_F is the Fermi energy.

It is important that the factor in Eq. (1) is taken from low-temperature measurements [40]. This factor characterizes the electron–phonon coupling constant and is used in the theory of superconductivity [10, 38, 39]. This generalization eliminates the difference between bands of the electron spectrum and the function $g_\Sigma(\varepsilon)$ for the total (subscript Σ) electron density of states is substituted into Eq. (1). Meanwhile, the d band of gold is located deep (about 2 eV) below the Fermi level and is not manifested at cryogenic temperatures. Consequently, the d band does not contribute to the factor in Eq. (1).

In other calculations [30–32, 40, 41] of the coefficient α cited above, the contributions of bands are separated, e.g., $\alpha_\Sigma = \alpha_s + \alpha_d$ for gold (see [40]). In this case, the α_Σ values are smaller [30–32, 40, 42] than those calculated by Eq. (1) (see, e.g., [42, Fig. 2]). We also note that the magnitude of $\alpha_\Sigma(T_e)$ significantly depends on the chosen screening [43]. We used four types of screening (Thomas–Fermi, Lindhard, Hubbard, and Singwi–Sjoelander); the Thomas–Fermi and Lindhard formulas give close results and the Singwi–Sjoelander screening is apparently the best (see [43, p. 6]).

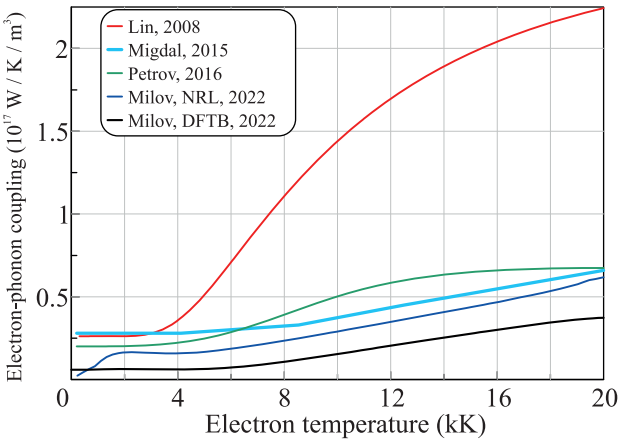

Fig. 1. (Color online) Theoretical dependences $\alpha_\Sigma(T_e)$, see the main text.

Figure 1 presents theoretical dependences $\alpha_\Sigma(T_e)$ taken from (red line) [10], (green line) [23], (sky blue line) [43, Fig. 7a], and (blue and black lines) [32, Fig. 1a]. As seen, the function $\alpha(T_e)$ from [10] begins to increase sharply according to Eq. (1) after an increase in the electron temperature T when d electrons and holes are involved in the electron–hole coupling. In our two-temperature hydrodynamic calculations reported below, we used the dependence $\alpha_\star(T_e)$ from [23] (green line in Fig. 1). We varied the electron–hole coupling constant using the factor n:

$$\alpha_\star \to \alpha_\star/n. \qquad (2)$$

The factor n in Eq. (2) is chosen such that the time dependence of the normalized correction to the reflection coefficient

$$-\Delta R/R_0, \quad \Delta R = R(t) - R_0, \qquad (3)$$

which is determined in the numerical simulation, reproduces our TTR measurements reported below. In Eq. (3), R_0 is the reflection coefficient before laser irradiation and $R(t)$ is the reflection coefficient as a function of the time before, during, and after laser irradiation.

3. THERMAL CONDUCTIVITY UNDER TWO-TEMPERATURE CONDITIONS

The theory of the thermal conductivity κ in two-temperature states is more complicated than the theory of the electron–hole heat exchange coefficient α. The number of calculations of κ is smaller [40, 42, 44–47]. Meanwhile, as mentioned above, heat stored in the skin layer of a bulk gold target during the ultrashort pulse is removed primarily owing to the thermal con-

ductivity. The thermal conductivity is the dominant mechanism of a decrease in the electron temperature in the skin layer. The cooling channel through the electron–hole coupling α is less important.

Dependences $\kappa(T_e, T_i)$ are shown in Fig. 2, where the dotted lines marked as Smirnov are taken from [47, Fig. 9] and the two solid lines were obtained within the model developed in [48]. This model was also used in our two-temperature hydrodynamic calculations. Within the model from [48], contributions to the thermal conductivity from the electron–electron, κ_{ee}, and electron–ion, κ_{ei}, collisions are calculated.

The thermal conductivity κ_{2T} is determined from these partial contributions using the Matthiessen's rule of summation of thermal resistivities

$$1/\kappa_{2T} = 1/(k_e\kappa_{ee}) + 1/\kappa_{ei}. \quad (4)$$

Here, k_e is an additional parameter used to vary the electron–electron contribution κ_{ee} to the thermal conductivity κ_{2T} in hydrodynamic calculation for the best description of experimental data: the larger the parameter, the smaller the contribution κ_{ee}.

We consider the single-temperature situation $T_e = T_i$ in the temperature range from the Debye temperature to the melting temperature, where thermal conductivity calculated within our model [48] weakly depends on the temperature: $\kappa_{2T} \approx \kappa_0$, where κ_0 is the thermal conductivity at room temperature, because an increase in the electron thermal conductivity $c_e \propto T_e$ in this range is compensated by an increase in the frequency of electron–hole collisions $\nu_{ei} \propto T_i$; $\nu_{ee} \ll \nu_{ei}$ at these temperatures.

The thermal conductivity κ was calculated in [47] disregarding electron–electron collisions with the frequency ν_{ee}. For this reason, the dotted lines shown in Fig. 2 are proportional to each other with the coefficient of proportionality equal to the ratio of ion temperatures T_i. In our model, the frequency ν_{ee} plays an important role.

The thermal conductivity κ under two-temperature conditions in theory increases strongly with the temperature T_e (cf. lines in Fig. 2 and the dashed line) because the electron specific heat c_e increases owing to a partial removal of degeneracy under the heating of the electron subsystem. The increase rate of the thermal conductivity κ_{2T} caused by an increase in the specific heat c_e because of increasing T_e decreases owing to an increase in the frequency ν_{ee}. The frequency ν_{ee} at high temperatures T_e increases slightly more slowly than T_e^2 (see Figs. 8 and 10 in [44]).

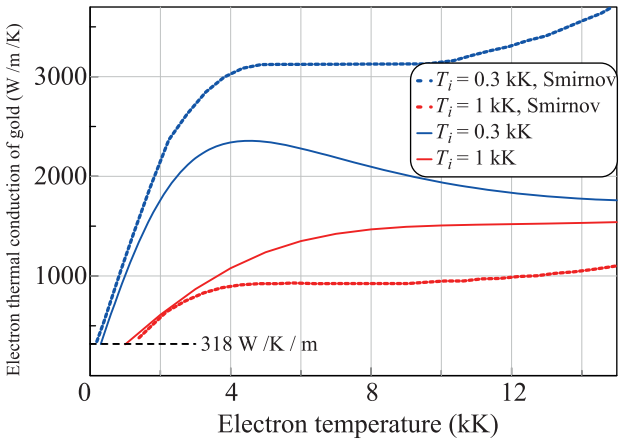

Fig. 2. (Color online) Theoretical dependences $\kappa(T_e, T_i)$. The dotted lines marked as Smirnov are taken from [47, Fig. 9]. The solid lines are obtained in the two-temperature hydrodynamic calculations in this work within our thermal conductivity model [48]. The horizontal dashed line indicates the thermal conductivity κ_0 at room temperature.

4. TWO-TEMPERATURE HYDRODYNAMIC SIMULATION

We used our two-temperature hydrocode verified in previous problems (see, e.g., [49]). The system of equations of two-temperature hydrodynamics was presented in [49]. To solve it, it is necessary to know the equation of state and the coefficients α and κ. The ion part of the equation of state for gold is described by the wide-range multiphase equation of state [50–52], whereas the electron part of the equation of state is taken according to [53]. The coefficients α and κ were presented in Sections 2 and 3 and Eq. (4). The absorption coefficient of gold at a pump wavelength of 400 nm and an angle of incidence of 45° is 0.7 (see the description of the experiment in [54] and Section 6 below). The Gaussian approximation of the time dependence of the experimental pump pulse gives a pulse duration of 150 fs at the $1/e$ level.

Figure 3 illustrates results of the numerical simulation. We performed about a hundred two-temperature hydrodynamic calculations with the parameters n and k_e in Eqs. (2) and (4), respectively, chosen for the best agreement with TTR measurements (3). The quasiadiabatic decrease in the temperature T_i on the surface in the first picoseconds is due to the stretching of a thin surface layer by the electron pressure. The heating of ions in this layer caused by the electron–ion coupling α at these short times is smaller than adiabatic cooling.

The calculations reported in Fig. 3 were performed for absorbed fluences F_{abs} = 7.42, 22.6, and 44.52 mJ/cm^2 corresponding to the weak, medium, and strong laser actions, respectively. The best agreement of these calculations with experimental data

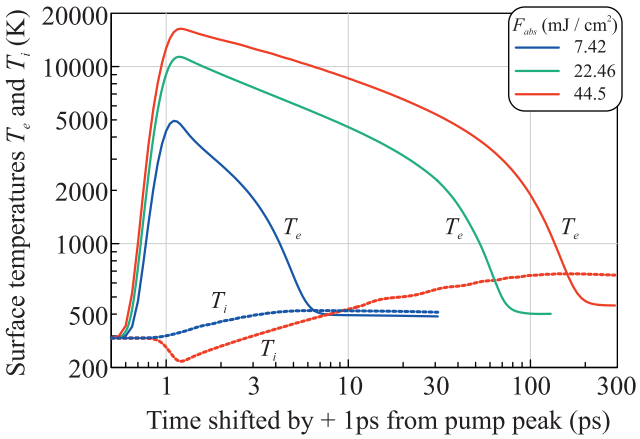

Fig. 3. (Color online) Time dependences of the electron and ion temperatures on the surface obtained in calculations consistent with the measured reflection coefficient (3). It is seen that the maximum of the ion temperature even under the most intense action is much lower than the gold melting temperature of 1337 K.

obtained for these fluences is achieved with the parameters $(n, k_e) = (0.5, 0.25)$, (9, 4.5), and (15, 7.5), respectively, which correct the dependences $\alpha(T_e)$ and $\kappa(T_e, T_i)$. As shown in the next section, the proportional variation of the parameters n and k_e does not change the temperature at the single-temperature stage (i.e., at long times).

Dependences (3) in our experiments were measured for a bulk target (1 mm thick) to a time of 340 ps. The length of the computational segment of 4 μm is sufficient for the numerical simulation of the bulk target in the time interval up to 350 ps.

5. TWO-TEMPERATURE THERMAL PROBLEM. ESTIMATES

The most important characteristics of the flow generated by the ultrashort laser pulse are the heating depth (in nanometers)

$$d_T \sim 90\frac{\gamma_{100}^{1/5}\chi_{10}^{2/5}}{\alpha_{17}^{2/5}}F_{100}^{1/5} \quad \text{or} \quad 65\frac{\gamma_{100}^{1/6}\chi_{10}^{1/3}}{\alpha_{17}^{1/3}}F_{100}^{1/6} \qquad (5)$$

at the two-temperature stage and the duration of this stage (in picoseconds) [49]

$$t_{eq} \sim 8\frac{\gamma_{100}^{2/5}}{\chi_{10}^{1/5}\alpha_{17}^{4/5}}F_{100}^{2/5} \quad \text{or} \quad 4\frac{\gamma_{100}^{1/3}}{\chi_{10}^{1/3}\alpha_{17}^{2/3}}F_{100}^{1/3}. \qquad (6)$$

Here, $\gamma_{100} = \gamma/100$ J m^{-3} K^{-2}, $c_e = \gamma T_e$ is the electron specific heat, $\alpha_{17} = \alpha/10^{17}$ W m^{-3} K^{-1}, $\chi_{10} = \chi_{2T}/10$ cm^2/s, $\chi = \kappa/c_e$ is the electron thermal diffusivity, $F_{100} = F_{abs}/100$ mJ/cm^2, and the left and right expressions are obtained with two slightly different approximations of solutions of the two-temperature heat transfer problem with losses [49].

According to Eqs. (5) and (6), the depth d_T and duration t_{eq} at fixed parameters γ and F_{abs} are determined by the coefficients α and κ_{2T}. It is important that the proportional variation of the coefficients α and κ_{2T} does not change the d_T value! If d_T remains unchanged, the temperature at the single-temperature stage ($T_e = T_i$) does not change at a fixed absorbed fluence F_{abs} (energy conservation law) because the temperature is determined by the volume energy density F_{abs}/d_T.

The duration of the two-temperature stage given by two approximations in Eqs. (6) increases

$$t_{eq} \propto n^{4/5}k_e^{1/5} \quad \text{or} \quad n^{2/3}k_e^{1/3} \qquad (7)$$

with the parameters n and k_e in Eqs. (2) and (4), respectively, which reduce electron–hole relaxation and electron thermal conductivity. The heating depth d_T and duration t_{eq} also increase slowly with the absorbed fluence F_{abs} according to Eqs. (5) and (6), respectively.

6. EXPERIMENT

The source of radiation was a Ti:S laser system (Legend, Coherent) generating 60-fs pulses with a repetition frequency up to 1 kHz. The time dynamics of TTR was measured using the pump–probe technique, the phase-sensitive detection method, and an SR830 Stanford Research Systems Lock-in Amplifier.

In this work, we implemented a specific regime of the measurement of a TTR signal at a low repetition frequency of pump pulses of 31.5 Hz, which were amplified in a regenerative amplifier. This regime allowed us to minimize collection effects and to obtain new data at higher radiation intensities and temperatures without the decomposition and degradation of the target compared to conventionally used regimes of the TTR measurement with a pulse repetition frequency of 80–100 MHz and a lattice heating temperature by several kelvins [55–60].

Pump pulses with a duration of 150 fs at a second harmonic wavelength of 400 nm were focused on a polycrystalline bulk gold sample at an angle of 45° into a 130 × 93-μm elliptic spot at the $1/e$ level. The measured integral reflection coefficient of the pump pulse from the target was 0.3. Probe pulses with a duration of 60 fs at a wavelength of 800 nm were focused normally into a spot 15 μm in diameter at the center of the heating region. The pump and probe pulses had a Gaussian spatial distribution.

An optical delay line was used to vary the time delay between the pump and probe pulses. The scanning steps were 100 fs in the interval from –2 to +5 ps, 1 ps in the interval from 5 to 105 ps, and 3.5 ps at times lon-

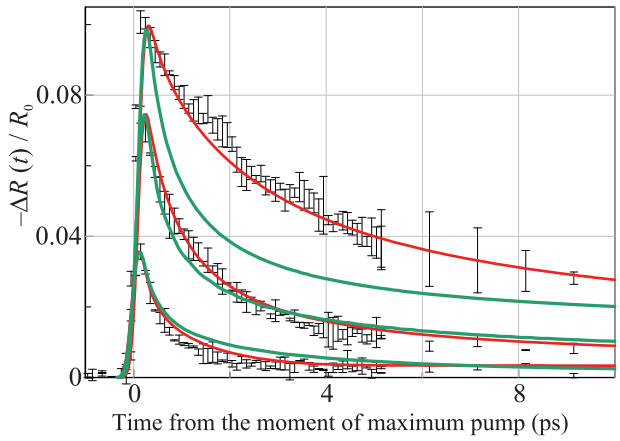

Fig. 4. (Color online) (Lines) Calculations and (vertical bars) transient thermoreflectance measurements. The top, middle, and bottom datasets are obtained under the strong, medium, and weak actions, respectively. The red lines are the best approximations of measurements. The green lines are obtained with the parameters α and κ close to those shown in Figs. 1 and 2; see the main text.

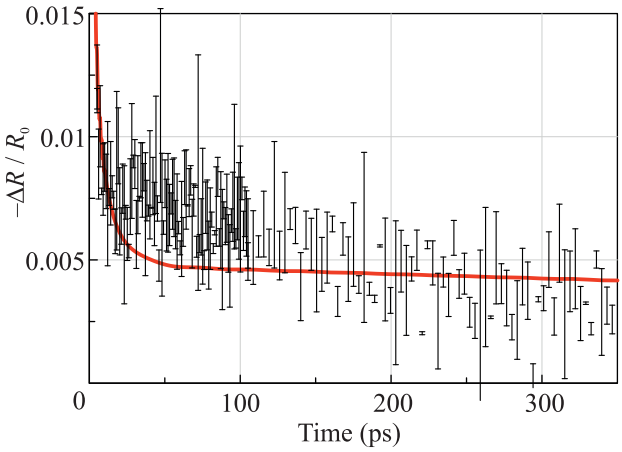

Fig. 5. (Color online) Same as in Fig. 4 but at long times under the medium action with the amplitude F_{abs} = 22.6 mJ/cm^2.

ger than 105 ps (see Figs. 4 and 5). Each vertical bar in Figs. 4 and 5 corresponds to one scanning step.

The time dependence of thermoreflectance (3) was measured at three absorbed fluences F_{abs} = 7.4, 22.1, and 44.3 mJ/cm^2. Two or three scans were recorded for each of these fluences with the subsequent averaging of the measured time dependences. Errors were determined as the standard deviation of these measurements and are indicated by vertical bars in Figs. 4 and 5. All measurements were carried out at one place on the target.

7. ANALYSIS AND DISCUSSION OF RESULTS

Figures 4 and 5 present the results of the numerical simulation in comparison with experimental data. It appeared that the experimental temperature at long times of ~100 ps for all three fluences is reproduced with a high accuracy at $n/k_e = 2$ (see an example in Fig. 5). For this reason, we fixed this ratio and varied the parameter n in order to reproduce a decrease in the reflection coefficient (3) at the two-temperature stage. The results are presented in Fig. 4.

Using the data presented in Fig. 4, we chose (n, k_e) = (0.5, 0.25), (9, 4.5), and (15, 7.5) for the weak, medium, and strong laser actions, respectively. These values correspond to the best approximations of experimental data shown by red lines in Fig. 4. As seen, in the case of strong action, there is a large correction in the direction of decrease for theoretical dependences of α and κ, which are shown in Figs. 1 and 2. At the same time, the α and κ values in the case of weak action are somewhat higher than the theoretical values.

The green line for strong action is obtained at the values (n, k_e) = (2, 1) close to the theoretical values in Figs. 1 and 2. A significant difference between the red and green lines in the case of strong action is seen in Fig. 4. This difference is much smaller in the case of medium action. The green line obtained at the values (n, k_e) = (2, 1) in Fig. 4 in the case of medium action passes through the bottom edge of experimental data (cf. strong action). The red and green lines in Fig. 4 for weak action are obtained at the values (n, k_e) = (0.5, 0.25) and (2, 1), respectively.

These results are plotted in Fig. 6. The estimates of the coefficient α shown by crosses in Fig. 6 are obtained by comparing the numerical simulation and experimental data (see Figs. 4 and 5). To determine

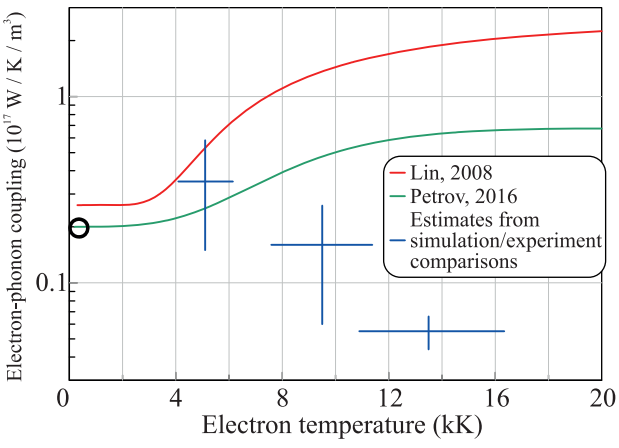

Fig. 6. (Color online) (Crosses) Estimated α values under weak, medium, and strong laser actions (see the main text) compared to the theoretical dependences from Fig. 1. The circle marks the α value obtained in old transient thermoreflectance measurements [11–14] under weak heating.

the spread of temperatures T_e (the horizontal segment of a cross), we took the maximum temperature T_e in Fig. 3 and 2/3 of this value.

To determine the bottom and top points of the vertical segment of the cross, we took three $\alpha(T_e|_{max})$ values, where $T_e|_{max}$ is the maximum value of T_e from Fig. 3, according to the green lines marked as Petrov, 2016 [23] in Figs. 1 and 6 for weak, medium, and strong actions. The indicated $\alpha(T_e|_{max})$ values were divided by n according to Eq. (2). The top and bottom points of the vertical segment were divided by n for the red and green lines in Fig. 4.

8. CONCLUSIONS

To summarize, we have performed numerous two-temperature numerical calculations and pump–probe TTR measurements with lock-in detection in the absorbed fluence range from 7 to 45 mJ/cm^2. A new laser action regime with a low repetition frequency of intense femtosecond pulses, which has not yet implemented in such experiments, allows us to significantly reduce the absorbed fluence compared to preceding experiments with megahertz trains of low-intensity pulses. The maximum temperature at the single-temperature stage exceeds half the melting temperature (see the time dependence of the ion temperature $T_i(t)$ shown by the red dotted line in Fig. 3).

A significant decrease in the most important parameters α and κ of two-temperature physics has been revealed at high temperatures (see Fig. 6). This decrease correlates with $\alpha(T_e)$ data recently obtained in [37] (see Fig. 9 in [37]) at fluences F_{abs} above the melting threshold. The thermodynamics and kinetics of melting were studied in [33–37] with ultrathin films (with thicknesses of about the thickness of the skin layer). In this case, an important problem of the thermal conductivity remains beyond our attention. The both most important parameters of two-temperature physics have been determined in this work. The parameter α under strong action decreases together with the two-temperature contribution κ_{ee} to the thermal conductivity κ_{2T} (see Section 3).

Thus, a hidden objection to a decrease in the parameter α is removed. Indeed, at small α values and standard (i.e., high) κ values (see Fig. 2), the absorbed fluence F_{abs} is diffused deep in the target. Correspondingly, the threshold of thermomechanical (spall) ablation $F_{abs}|_{abl}$ and the crater depth $d_{crat}|_{abl}$ at this threshold for gold are much larger than the known theoretical and experimental values $F_{abs}|_{abl} \simeq 0.2$ J/cm^2 and $d_{crat}|_{abl} \simeq 0.1$ μm (see [61, 62]). If the parameters α and κ_{2T} are reduced proportionally to each other, the threshold values hold together with the maximum ion temperature T_i and the volume energy density F_{abs}/d_T at the single-temperature stage.

FUNDING

This work was supported by the Russian Science Foundation (project no. 19-19-00697-P prolonged).

CONFLICT OF INTEREST

The authors declare that they have no conflicts of interest.

REFERENCES

1. V. V. Temnov, C. Klieber, K. A. Nelson, T. Thomay, V. Knittel, A. Leitenstorfer, D. Makarov, M. Albrecht, and R. Bratschitsch, Nat. Commun. **4**, 1468 (2013).
2. X. W. Wang, A. A. Kuchmizhak, X. Li, S. Juodkazis, O. B. Vitrik, Yu. N. Kulchin, V. V. Zhakhovsky, P. A. Danilov, A. A. Ionin, S. I. Kudryashov, A. A. Rudenko, and N. A. Inogamov, Phys. Rev. Appl. **8**, 044016 (2017).
3. R. Fang, A. Vorobyev, and Ch. Guo, Light Sci. Appl. **6**, e16256 (2017).
4. I. N. Saraeva, S. I. Kudryashov, A. A. Rudenko, M. I. Zhilnikova, D. S. Ivanov, D. A. Zayarny, A. V. Simakin, A. A. Ionin, and M. E. Garcia, Appl. Surf. Sci. **470**, 1018 (2019).
5. N. A. Smirnov, S. I. Kudryashov, A. A. Rudenko, A. A. Nastulyavichus, and A. A. Ionin, Laser Phys. Lett. **19**, 026001 (2022).
6. V. V. Shepelev, Yu. V. Petrov, N. A. Inogamov, V. V. Zhakhovsky, E. A. Perov, and S. V. Fortova, Opt. Laser Technol. **152**, 108100 (2022).
7. N. A. Inogamov, V. V. Zhakhovskii, and V. A. Khokhlov, J. Exp. Theor. Phys. **127**, 79 (2018).
8. M. I. Kaganov, I. M. Lifshitz, and L. V. Tanatarov, Sov. Phys. JETP **4**, 173 (1957).
9. S. I. Anisimov, B. L. Kapeliovich, and T. L. Perel'man, Sov. Phys. JETP **39** (2), 375 (1974).
10. Zh. Lin, L. V. Zhigilei, and V. Celli, Phys. Rev. B **77**, 075133 (2008).
11. S. D. Brorson, J. G. Fujimoto, and E. P. Ippen, Phys. Rev. Lett. **59**, 1962 (1987).
12. S. D. Brorson, A. Kazeroonian, J. S. Moodera, D. W. Face, T. K. Cheng, E. P. Ippen, M. S. Dresselhaus, and G. Dresselhaus, Phys. Rev. Lett. **64**, 2172 (1990).
13. T. Juhasz, H. E. Elsayed-Ali, G. O. Smith, C. Suárez, and W. E. Bron, Phys. Rev. B **48**, 15488 (1993).
14. S.-S. Wellershoff, J. Hohlfeld, J. Guedde, and E. Matthias, Appl. Phys. A **69** (Suppl. 1), S99 (1999).
15. B. J. Siwick, J. R. Dwyer, R. E. Jordan, and R. J. D. Miller, Science (Washington, DC, U. S.) **302** (5649), 1382 (2003).
16. R. Ernstorfer, M. Harb, Ch. T. Hebeisen, G. Sciaini, Th. Dartigalongue, and R. J. D. Miller, Science (Washington, DC, U. S.) **323** (5917), 1033 (2009).
17. J. Chen, W.-K. Chen, J. Tang, and P. M. Rentzepis, Proc. Natl. Acad. Sci. U. S. A. **108**, 18887 (2011).
18. K. Widmann, T. Ao, M. E. Foord, D. F. Price, A. D. Ellis, P. T. Springer, and A. Ng, Phys. Rev. Lett. **92**, 125002 (2004).

19. Y. Ping, D. Hanson, I. Koslow, T. Ogitsu, D. Prendergast, E. Schwegler, G. Collins, and A. Ng, Phys. Rev. Lett. **96**, 255003 (2006).
20. T. Ao, Y. Ping, K. Widmann, D. F. Price, E. Lee, H. Tam, P. T. Springer, and A. Ng, Phys. Rev. Lett. **96**, 055001 (2006).
21. Y. Ping, D. Hanson, I. Koslow, T. Ogitsu, D. Prendergast, E. Schwegler, G. Collins, and A. Ng, Phys. Plasmas **15**, 056303 (2008).
22. Z. Chen, B. Holst, S. E. Kirkwood, V. Sametoglu, M. Reid, Y. Y. Tsui, V. Recoules, and A. Ng, Phys. Rev. Lett. **110**, 135001 (2013).
23. S. I. Ashitkov, P. S. Komarov, V. V. Zhakhovsky, Yu. V. Petrov, V. A. Khokhlov, A. A. Yurkevich, D. K. Ilnitsky, N. A. Inogamov, and M. B. Agranat, J. Phys.: Conf. Ser. **774**, 012097 (2016).
24. K. Sokolowski-Tinten, Ch. Blome, J. Blums, A. Cavalleri, C. Dietrich, A. Tarasevitch, I. Uschmann, E. Foerster, M. Kammler, M. H. von Hoegen, and D. von der Linde, Nature (London, U.K.) **422**, 287 (2003).
25. D. S. Ivanov and L. V. Zhigilei, Phys. Rev. B **68**, 064114 (2003).
26. N. A. Inogamov, V. V. Zhakhovskii, S. I. Ashitkov, V. A. Khokhlov, Yu. V. Petrov, P. S. Komarov, M. B. Agranat, S. I. Anisimov, and K. Nishihara, Appl. Surf. Sci. **255**, 9712 (2009).
27. L. V. Zhigilei, Zh. Lin, and D. S. Ivanov, J. Phys. Chem. C **113**, 11892 (2009).
28. V. V. Zhakhovskii, K. Nishihara, S. I. Anisimov, and N. A. Inogamov, JETP Lett. **71**, 167 (2000).
29. A. K. Upadhyay, N. A. Inogamov, B. Rethfeld, and H. M. Urbassek, Phys. Rev. B **78**, 045437 (2008).
30. N. Medvedev and I. Milov, Phys. Rev. B **102**, 064302 (2020).
31. N. Medvedev and I. Milov, Eur. Phys. J. D **75**, 212 (2021).
32. F. Akhmetov, N. Medvedev, I. Makhotkin, M. Ackermann, and I. Milov, Materials **15**, 5193 (2022).
33. M. Z. Mo, Z. Chen, R. K. Li, et al., Science (Washington, DC, U. S.) **360** (6396), 1451 (2018).
34. M. Mo, Zh. Chen, and S. Glenzer, MRS Bull. **46** (08) (2021).
35. J. M. Molina and Th. G. White, in *Proceedings of the 2021 IEEE International Conference on Plasma Science ICOPS* (2021), p. 1. https://doi.org/10.1109/ICOPS36761.2021.9588426
36. J. M. Molina and T. G. White, Matter Radiat. Extremes **7**, 036901 (2022).
37. M. Arefev, M. Shugaev, and L. Zhigilei, Sci. Adv. **8**, eabo2621 (2022).
38. X. Y. Wang, D. M. Riffe, Y. S. Lee, and M. C. Downer, Phys. Rev. B **50**, 8016 (1994).
39. P. B. Allen, Phys. Rev. Lett. **59**, 1460 (1987).
40. Yu. V. Petrov, N. A. Inogamov, and K. P. Migdal, JETP Lett. **97**, 20 (2013).
41. K. P. Migdal, Y. V. Petrov, and N. A. Inogamov, SPIE Proc. **9065**, 906503 (2013).
42. K. P. Migdal, Yu. V. Petrov, D. K. Il'nitsky, V. V. Zhakhovsky, N. A. Inogamov, K. V. Khishchenko, D. V. Knyazev, and P. R. Levashov, Appl. Phys. A **122**, 408 (2016).
43. K. P. Migdal, D. K. Il'nitsky, Yu. V. Petrov, and N. A. Inogamov, J. Phys.: Conf. Ser. **653**, 012086 (2015).
44. N. A. Inogamov and Yu. V. Petrov, J. Exp. Theor. Phys. **110**, 446 (2010).
45. D. V. Knyazev and P. R. Levashov, Comput. Mater. Sci. **79**, 817 (2013).
46. Yu. V. Petrov, K. P. Migdal, D. V. Knyazev, N. A. Inogamov, and P. R. Levashov, J. Phys.: Conf. Ser. **774**, 012103 (2016).
47. N. A. Smirnov, Phys. Rev. B **106**, 024109 (2022).
48. Yu. V. Petrov, N. A. Inogamov, S. I. Anisimov, K. P. Migdal, V. A. Khokhlov, and K. V. Khishchenko, J. Phys.: Conf. Ser. **653**, 012087 (2015).
49. N. A. Inogamov, V. V. Zhakhovskii, and V. A. Khokhlov, J. Exp. Theor. Phys. **120**, 15 (2015).
50. A. V. Bushman, G. I. Kanel', A. L. Ni, and V. E. Fortov, *Intense Dynamic Loading of Condensed Matter* (Taylor and Francis, Washington, D.C., 1993).
51. K. V. Khishchenko, S. I. Tkachenko, P. R. Levashov, I. V. Lomonosov, and V. S. Vorobev, Int. J. Thermophys. **23**, 1359 (2002).
52. I. V. Lomonosov, Laser Part. Beams **25**, 567 (2007).
53. Yu. V. Petrov, K. P. Migdal, N. A. Inogamov, and V. V. Zhakhovsky, Appl. Phys. B **119**, 401 (2015).
54. S. I. Ashitkov, N. A. Inogamov, P. S. Komarov, Yu. V. Petrov, S. A. Romashevskii, D. S. Sitnikov, E. V. Struleva, and V. A. Khokhlov, High Temp. **60** (2022, in press).
55. A. Block, M. Liebel, R. Yu, M. Spector, Y. Sivan, F. J. García de Abajo, and N. F. van Hulst, Sci. Adv. **5**, eaav8965 (2019).
56. P. M. Norris, A. P. Caffrey, R. J. Stevens, J. M. Klopf, J. T. McLeskey, and A. N. Smith, Rev. Sci. Instrum. **74**, 400 (2003).
57. E. L. Radue, J. A. Tomko, A. Giri, J. L. Braun, X. Zhou, O. V. Prezhdo, E. L. Runnerstrom, J.-P. Maria, and P. E. Hopkins, ACS Photon. **5**, 4880 (2018).
58. P. E. Hopkins, J. M. Klopf, and P. M. Norris, Appl. Opt. **46**, 2076 (2007).
59. P. E. Hopkins and P. M. Norris, Appl. Surf. Sci. **253**, 6289 (2007).
60. P. Jiang, X. Qian, and R. Yang, J. Appl. Phys. **124**, 161103 (2018).
61. N. A. Inogamov, V. V. Zhakhovskii, S. I. Ashitkov, Yu. V. Petrov, M. B. Agranat, S. I. Anisimov, K. Nishihara, and V. E. Fortov, J. Exp. Theor. Phys. **107**, 1 (2008).
62. B. J. Demaske, V. V. Zhakhovsky, N. A. Inogamov, and I. I. Oleynik, Phys. Rev. B **82**, 064113 (2010).

Translated by R. Tyapaev

SPELL: OK